Publishing House
AKAPIT

COMPUTER METHODS IN MATERIALS SCIENCE
Informatyka w Technologii Materiałów

Vol. 10, 2010, No. 4

NUMERICAL AND EXPERIMENTAL STUDIES OF THE STRENGTH OF RIVETED JOINTS

Nanjiang Chen[1, 2], Jean-loup Chenot[1], Min Wan[2], Julien Malrieu[3],
Maxime Thonnerieux[3], Richard Ducloux[4]

[1] CEMEF – Mines ParisTech, BP 207 – 06904 Sophia Antipolis Cedex, France
[2] School of Mechanical Engineering and Automation, Beihang University, 100191, P. R China
[3] Cetim Saint Etienne, 7 rue de la presse, 42952, Saint Etienne, France
[4] Transvalor, Les Espaces Delta, BP 037 Sophia Antipolis Cedex / France
**Corresponding author: nanjiang.chen@mines-paristech.fr or chennanjiang@me.buaa.edu.cn*

Abstract

In general, there are two main types of failure observed in solid riveted joints: tensile failure and shear failure. To study these phenomena, four sizes of riveted joints are utilized to do the riveting, tension and shear process. Meanwhile, corresponding FEM models are built in Forge® 2009 to simulate each process for these joints. In the simulations, Bauschinger Effect of the rivet material is taken into account to obtain more accurate simulation results. Based on Oyane et al. (1980) and Cockcroft and Latham (1968) damage criteria, a new damage model in which the first principle stress and hydrostatic pressure are both considered is proposed to predict the fracture initiation and growth in the tension and shear process of riveted joints. The results from the simulations are in quite good compared with those from the experiments.

Key words: riveted joints, solid rivet, strength, finite element

1. INTRODUCTION

As one of mechanical fastener joints, riveted joints are widely used in industry including the aerospace industry, vehicles, bridges and many others fields. In general there are two types of failure observed in mechanical fasteners: shear failure and tensile failure (Kelly & Costello, 2004). Engineers usually utilize a series of practical tests to obtain the strength of the riveted joints which is time consuming and costly. In recent years, with the development of the Finite Element Method (FEM) and computing technology, most mechanical problems such as bulk forming, sheet forming and many others processes can be simulated with FEM softwares which may save much time and reduce or avoid expensive laboratory experiments for the companies. Furthermore, with a FEM software, a better insight of the process is possible by analyzing the various mechanical parameters in the volume which make it easier to modify parameters in order to achieve a good result. For the riveted joints, a very large number of research papers can be found in the literatures which cover almost every kind of rivet such as the solid rivet, blind rivets and self-pierce rivet.

Kelly and Costello (2004) simulated the riveting and uniaxial tension process of one kind of aluminium blind rivets by using an axisymmetric model and compared the shape of the riveted joint and the load with the results from the experiments. They found that because the actual rivets couldn't always set symmetrically, the results from the axisymmetric simulation were a little different from the results from the experiments (Kelly & Costello, 2004).

259 – 270 ISSN 1641-8581

Bouchard et al simulated the self-pierce riveting process in Forge2005® which involved solving numerical difficulties such as damage, fracture and contact between deformable bodies. The results from the simulation showed a good agreement with those from the physical tests (Bouchard et al., 2008). Blanchot and Daidie (2006) utilized slice (15° sector), axisymmetric and symmetric models to simulate the riveting process of the countersunk rivet with 4mm diameter and 9mm initial length and showed the strain and stress distribution in the rivet and the sheets after the riveting process (Blanchot & Daidie, 2006). Ryan and Monaghan (2000) studied the failure mechanism of the riveted joint in fibre metal laminates using a countersunk rivet.

However, a systematic and comprehensive study based on the comparison of numerical and experimental data of several different sizes of rivets is very scarce if any in the literature. Such kind of study is necessary to give confidence in the results of numerical simulation which is the major concern of the industry to use it routinely in the early stage of design (Chen et al., 2010). In the previous study (Chen et al., 2010), the authors have built the FEM models of four sizes of solid rivets (the diameters of the rivets are 14.9 mm, 11.6 mm, 9.8 mm and 5.8 mm) and simulated the riveting process of these rivets in Forge2008®. The results from the simulation, including the punch force displacement curves, the hardness distributions and the final shape of the riveted joints are quite good compared with the results from the experiments.

In order to study the strength of the riveted joints, further simulations and experiments have to be done. Because the Bauschinger effect and kinematic hardening of the rivet material during the manufacturing and riveting process, it is necessary to treat the rivet material differently in riveting and tensile or shearing processes. During the tension and shearing process of the riveted joints, the rivet will undergo fracture and then breaks, so the material of the rivet has to include the damage property in the simulation. Hence, the main activities in this paper deals with the following aspects:

1. identification of the constitutive parameters of the rivet material;
2. short description of the damage model used in the simulation;
3. simulations and experiments of the tension and shearing of the riveted joints;
4. comparison of results of the tension and shearing from the simulation and shearing.

2. FINITE ELEMENT METHOD

For a more complete description of the scientific approach of FE simulation of metal forming process, the reader may refer to (Wagoner & Chenot, 1996).

2.1. Constitutive equation

The total strain is decomposed into and elastic part $\boldsymbol{\varepsilon}^e$ and a plastic part $\boldsymbol{\varepsilon}^p$:

$$\varepsilon = \varepsilon^e + \varepsilon^p \tag{1}$$

The linear elastic Hooke's law is used to connect the stress tensor $\boldsymbol{\sigma}$ and elastic strain tensor $\boldsymbol{\varepsilon}^e$. Their time derivatives are related by the fourth order elasticity tensor $\boldsymbol{E}$.

$$\dot{\sigma} = E\dot{\varepsilon}^e \tag{2}$$

The plastic component of the strain rate tensor obeys the flow rule:

$$\sigma' = \frac{2}{3}\sigma_0(\bar{\varepsilon})\frac{\dot{\varepsilon}^p}{\dot{\bar{\varepsilon}}} \tag{3}$$

where σ' is the deviatoric stress tensor, σ_0 is the yield stress, $\dot{\bar{\varepsilon}}$ is the equivalent strain rate and $\bar{\varepsilon}$ is the equivalent strain.

In order to correct the stresses rate for rotations, the Jaumann derivative of the stress tensor is used in equation (4):

$$\frac{d_J\sigma}{dt} = \dot{\sigma} - \dot{\omega}\sigma + \sigma\dot{\omega} \tag{4}$$

where $\dot{\omega}$ is the spin tensor.

2.2. Friction

At the interface between part and tool the friction shear stress can be modeled by a Coulomb's law:

$$\tau = -\alpha_f \,|\, \sigma_n \,|\, \frac{\Delta v}{|\,\Delta v\,|} \quad \text{with } |\,\tau\,| \leq \frac{\sigma_0}{\sqrt{3}} \tag{5}$$

where α_f is the friction coefficient, σ_n is the normal stress and Δv is the tangential velocity difference between part and tool.

2.3. The virtual work principle

The virtual work principle states that the virtual work of the external forces is equal to the virtual work of the internal forces:

$$\int_{\partial\Omega} \sigma n \delta u dS - \int_{\Omega} div(\sigma)\delta u dV = \int_{\Omega} \sigma \delta \varepsilon dV \qquad (6)$$

where, Ω is a finite domain with boundary $\partial\Omega$, ρ is the mass density, δu is a virtual displacement field and $\delta\varepsilon$ is the corresponding virtual strain tensor.

The mass conservation equation is:

$$-\int_{\Omega} (\kappa div(v) + \dot{p})\delta p dV = 0 \qquad (7)$$

where κ is the compressibility coefficient of the material, δp is any virtual pressure field.

The most widely used time integration method remains the simple one step Euler scheme. In this simple approach, the total time is decomposed into small increments Δt and the displacement field is proportional to the velocity field at the beginning of the increment:

$$\Delta u = \Delta t \text{ v} \qquad (8)$$

In the same way the stress increments are introduced, so that equations (9) and (10) are rewritten:

$$\int_{\Omega} (\sigma' + \Delta\sigma') : \delta\dot{\varepsilon} dV = \int_{\Omega} (p + \Delta p) div(\delta v) dV + \int_{\partial\Omega_c} \tau \delta v dS \qquad (9)$$

$$-\int_{\Omega} (\kappa div(\Delta u) + \Delta p)\delta p dV = 0 \qquad (10)$$

2.4. Contact formulation

We followed the same approach as Forge2008® which can deal with multi-body and multi-material structures. A nodal incremental form of the penalty technique is used for contact analysis. At each time step, the nodes that are potentially going to penetrate the opposite surface are searched. Based on the in-depth penetration measurement, a penalty contribution is added to the functional for these nodes. The contact terms arising from contact between different bodies are computed through a coupled approach based on a master-slave algorithm (Bouchard et al., 2008).

$$b(\lambda, u) = \int_{\Gamma^C} \lambda h(u_a, u_b) ds \qquad (11)$$

where, Γ^c is the contact surface, λ is the contact normal stress and $h(u_a, u_b)$ is the distance function between the two contact surfaces.

However, after finite element discretization, the two surfaces are not similar, so it is necessary to define on which surface the right part of equation (11) should be integrated.

In the usual master/slave formulations, $b(\lambda, u)$ is only integrated on the slave body surface:

$$b(\lambda_a^h, u^h) = \int_{\Gamma_a^C} \lambda_a^h h(u_a^h, u_b^h) ds \qquad (12)$$

where, λ_a^h is the normal stress on the slave body surface, while Γ_a^C is the slave body surface.

In order to obtain an accurate integration result, the slave body should be discretized more finely than the master body, but that is not always possible in the reality. Hence, the symmetric formulation was proposed in which the integration happens in both surfaces:

$$b(\lambda^h, u^h) = \frac{1}{2}\left(\int_{\Gamma_a^C} \lambda_a^h h(u_a^h, u_b^h) ds + \int_{\Gamma_b^C} \lambda_b^h h(u_b^h, u_a^h) ds \right) \qquad (13)$$

However, if the discretizations of the two surfaces are similar then this method will introduce too many contact conditions and may artificially stiffen the contact interface.

Consequently, in the quasi-symmetric formulation, λ_b^h is replaced by an approximation $\tilde{\lambda}_b^h$ that is calculated from λ_a^h only:

$$b(\lambda^h, u^h) = \frac{1}{2}\left(\int_{\Gamma_a^C} \lambda_a^h h(u_a^h, u_b^h) ds + \int_{\Gamma_b^C} \tilde{\lambda}_b^h h(u_b^h, u_a^h) ds \right) \qquad (14)$$

where, $\tilde{\lambda}_b^h$ is equal to $\pi_b^h(\lambda_a^h)$ which is the orthogonal projection of λ_a^h on Γ_a^C (Fourment, 2008).

2.5. Finite element discretization

The geometric domain Ω is discretized into a finite number of elements. In the present study isoparametric elements are utilized. A characteristic of these elements is that the same rule is applied to interpolate both the geometry and the independent field variables between the values in the nodes. The displacement field is discretized with tetrahedral linear shape functions N_n, in term of nodal displacement vectors U_n plus a bubble function N_b:

$$\Delta u = \sum_n \Delta U_n N_n(\xi) \qquad (15)$$

The strain increment tensor can be computed with the help of the conventional B discretized linear operator:

$$\Delta\varepsilon = \sum_n U_n B_n \tag{16}$$

The pressure field is discretized with only the linear shape functions:

$$\Delta p = \sum_n \Delta P_n N_n \tag{17}$$

Finally the discretized mixed integral formulation for the mechanical problem is:

$$R_n^U = \int_\Omega (\sigma' + \Delta\sigma') : B_n dV - \int_\Omega (p + \Delta p) trace(B_n) dV + \int_{\partial\Omega} \alpha_f |\sigma_n| \frac{\Delta v}{|\Delta v|} N_n dV = 0 \tag{18}$$

$$R_m^p = \int_\Omega (\kappa div(\Delta u) + \Delta p) M_m dV = 0 \tag{19}$$

Remark: at each time increment equation (18) is first written without the Jaumann correction on the stress increment and the system of equations (18) and (19) is solved. Then the stress tensor is transformed using the rotation matrix corresponding to the spin increment.

2.6. Other numerical issues

The non-linear equations resulting from the mechanical behaviour are linearized with the help of the Newton-Raphson method. The resulting linear systems are often solved now with iterative methods, which appear faster and require much less CPU memory than the direct ones.

Prediction of possible formation of folding defects during forging is based on the analysis of the contact of the part with itself, so providing a problem similar to the coupling with tools.

Automatic dynamic remeshing during the simulation of the whole forming process is almost always necessary, as elements undergo very high strain which could produce degeneracy. Before this catastrophic event, decrease of element quality must be evaluated and a remeshing module must be launched periodically to recover a satisfactory element quality. The global mesh can be completely regenerated, using a Delaunay or any front tracing method, but the method of iterative improvement of the mesh, with a possible local change of element structure and connectivity, seems to be much more effective.

For industrial complicated applications, with short delays, the computing time can be decreased dramatically using several or several tens of processors. This requires to use an iterative solver and to define a partition of the domain, each sub domain being associated with a processor. But the parallelization is made more complex due to remeshing and the remeshing process itself must be parallelized.

In order to avoid the necessity for the user to perform several computations, with different meshes to check the accuracy, error estimation can be developed using for example the generalization of the method proposed by Zienckiewicz and Zhu (1987). Then, if the rate of convergence of the approximation is known, the local mesh refinement necessary to achieve a prescribed tolerance can be computed, and the meshing modules are improved to be able to respect the refinement when generating the new mesh.

3. RIVET CONFIGURATION

Configuration of the riveted joint before assembly is illustrated in figure 1 and the sizes of the four riveted joints are shown in table 1.

Table 1. *Riveted joints parameters used in the study.*

Case	d (mm)	L (mm)	d_h (mm)	L_1 (mm)	L_2 (mm)
a	9.8	30.4	10.25	7.8	7.8
b	9.8	25.4	10.25	7.8	5.8
c	9.8	25.4	10.25	5.8	7.8
d	9.8	25.4	10.25	5.8	5.8

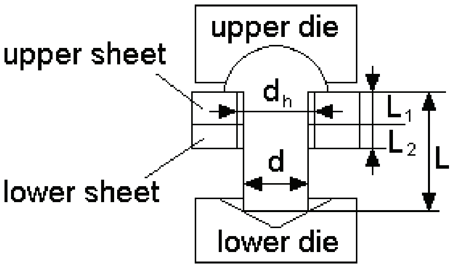

Fig. 1. *Configuration of riveted joint.*

4. RIVETING PROCESS

4.1. Material properties of the rivet and the sheets

During the riveting and tension process of the riveted joints, plastic deformation occurs mainly in the shank part of the rivet. Figure 2 shows the dynamic process of the rivet material used in the study. In the A process or the manufacturing process, the producer forms a rod into a rivet, so the rivet material is under a compressive stress. In the B process or the riveting process, the rivet material is also mainly under a compressive stress. In the C process or the tension process, which is scheduled to obtain the strength of the riveted joints, the rivet material is under a tensile stress. As a common phenomenon in metallic materials, the Bauschinger Effect is defined as that the strength of a material on forward loading (e.g. in compression) is reduced upon reverse loading (e.g. in tension) (Deng et al., 2005). Hence, building a proper material model of the rivet for the simulation is essential to achieve a result which is as close as possible to the reality. Three tests including a hardness test, a uniaxial tension test and an upset test are utilized to obtain constitutive parameters of the rivet material.

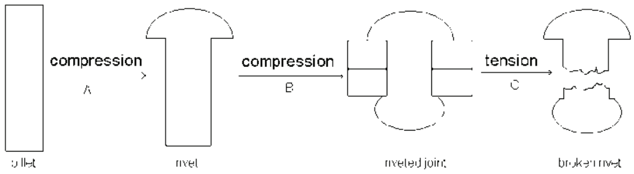

Fig. 2. Dynamic process of the rivet material used in the experiments.

Because it is not easy to get the original billet material which is used to produce the rivet, only the manufactured rivet can be utilized to do the uniaxial tension and the upset test. To ensure that the initial yield stress in the shank of the rivet is uniform, a rivet is cut into two pieces along the longitudinal direction and then a Vickers pyramid indentation is performed with a load of 30kgf. We obtain the hardness distribution on the section surface of the rivet as shown in figure 3. According to Tabor's study (1951) which has been verified by many other researchers (Boyer, 1987; Busby et al., 2005), the Vickers' hardness is proportional to the yield stress of the metals.

Table 2. *Vickers's hardness on the section of the rivet shank.*

Point	Point 1	Point 2	Point 3	Point 4	Point 5	Point 6
Hv	122	123	122	123	120	120

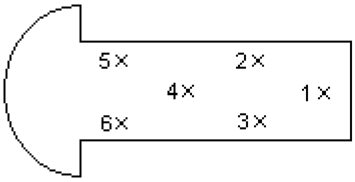

Fig. 3. Hardness indentation points distribution on the section.

Table 2 shows the values of hardness on the longitudinal section of the rivet. In table 2, it is obvious that the initial yield stress in the shank of the rivet is almost uniform.

Uniaxial tension and upset test are utilized to obtain the constitutive parameters of the rivet material. In figure 4, the left sample is machined from a rivet for the uniaxial tension test with 6mm in diameter and 15 mm in length while the right sample is for the upset test with the same diameter as the shank of the rivet and 12 mm in length.

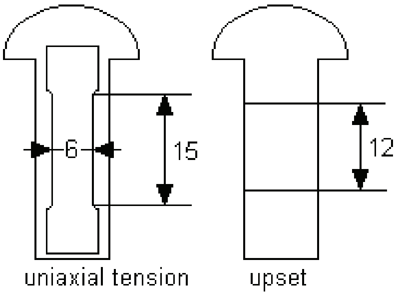

Fig. 4. Geometry of the sample cut from the rivet for the uniaxial tension (left) and upset tests (right).

Figure 5 shows the comparison of the true stress strain curves between the data from the uniaxial tension and the upset test for each case. In each figure, it is easy to find that before the necking point, the difference between the two curves is almost only a constant value, that is:

$$\sigma_{upset} - \sigma_{tension} = f_{upset}(\varepsilon) - f_{tension}(\varepsilon) \cong C, \quad \text{when } \varepsilon \le \varepsilon_{necking} \tag{20}$$

where, σ_{upset} is the equivalent stress when the equivalent strain is ε in the upset test while $\sigma_{tension}$ is that in the uniaxial tension test, $\varepsilon_{necking}$ is the equivalent strain at the necking point in the uniaxial tension test and C is constant value.

As aforementioned, because the rivet material is under compressive stress during the A process in Figure 2, these phenomenon can be attributed to the Bauschinger Effect. In the riveting process, the material of the rivet is mainly under a compressive stress, so the constitutive parameters from the upset test are utilized in the simulation.

Since the deformation of the sheets in the study is relatively small, only uniaxial tension tests are utilized to obtain the constitutive parameters of the sheets. Two kinds of sheets are used in the experiments: HLES600MC and HLES355MC. The thicknesses of them are 7.8 mm and 5.8 mm respectively. The Young's modulus and Poisson's ratio are 210 GPa and 0.3. For HLES600MC, the yield stress and the maximum stress are 600 MPa and 780 MPa and for HLE355MC, these two values are 380 MPa and 530 MPa.

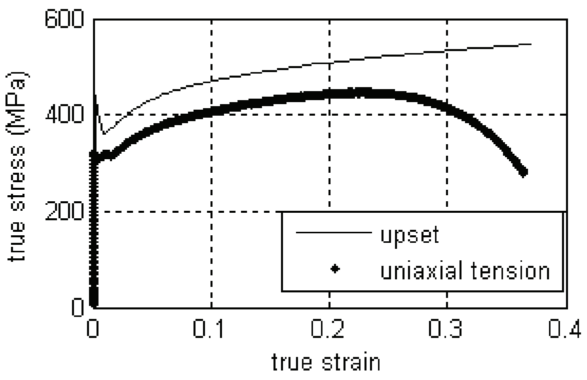

Fig. 5. True stress true strain curves obtained from the upset and the uniaxial tension tests for rivet.

4.2. Experiments and simulations

As shown in Figure 1, in experiments, the upper die is fixed and the lower die moves up to deform the rivet. The total displacements of the lower die for all of the four cases are 9.3 mm, 7 mm, 7 mm and 8.4 mm and the speed is set as 6 mm/s.

Because in a further parameter study, the rivet may be eccentric or lean on the inner walls of the sheets holes, 3D geometry is selected to develop the model rather than 2D in simulations. However, thanks to the symmetry of the riveting process, only one half of the rivet has to be modeled which can reduce computational time. In the simulation, Coulomb law is selected as the friction law between the contacted parts and the coefficient is set as 0.15.

Table 3. *Comparison of the forming head for each case.*

case	H_{head} (mm)			D_{head} (mm)		
	Experiment	Simulation	Error	Experiment	Simulation	Error
a	7.7	7.4	-3.9%	15.7	15.8	0.6%
b	6.6	6.5	-1.5%	15	15.4	2.7%
c	6.6	6.5	-1.5%	15.1	15.4	2.0%
d	7.1	7.0	-1.4%	15.4	15.9	3.3%

4.3. Results

In a riveted joint, the final shape of the forming head is the most important geometric parameter as it affects the strength of the joint. The height and the diameter of the head are the two parameters that are considered here to evaluate the head as shown in figure 6. Table 3 shows these values in each case for both the simulation and the experiment under the same lower die displacement. In order to reduce the random error in experiments, the average value of several samples is used as the final value in experiment for each case. For all the four cases, the biggest error is less than 4%.

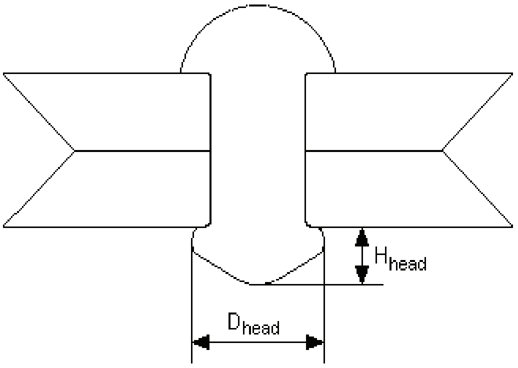

Fig. 6. *Two important parameters of the forming head.*

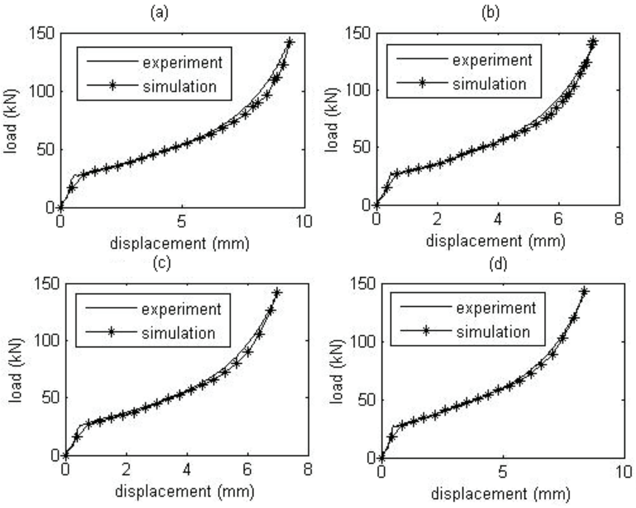

Fig. 7. *Load displacement curves during the riveting process for all cases.*

Figure 7shows the comparison of load displacement curves during the riveting process for all of the four riveted joints. The load here indicates the load of the press machine while the displacement corresponds to the lower die. The curve from the simulation is in very good agreement with experimental one for each case. It is noticed that after the yield of the rivet material, the slope of the curve increases because the diameter of the rivet increases under the compressive stress.

5. DUCTILE FRACTURE CRITERION IN TENSION AND SHEARING OF THE RIVETED JOINTS

In tension and shearing of riveted joints, ductile fracture occurs in the rivet and then breaks it. Therefore, ductile fracture criterion has to be taken into account in the simulations of these two processes. In recent years, researchers have proposed many criteria and applied them in finite element software.

The first category is commonly known as 'decoupled damage criterion' which neglects the influence of damage on the yield of the material. For this kind of criterion, materials are assumed to be continuous and isotropic throughout the deformation. When the integral of a function of stress tensor on plastic strain reaches a threshold value, fracture occurs in the material. It can be written as:

$$\int_0^{\bar{\varepsilon}_f} f(\sigma)d\bar{\varepsilon} = C \tag{21}$$

where, $\bar{\varepsilon}_f$ is the equivalent strain at the fracture point, σ is the stress tensor, $\bar{\varepsilon}$ is the equivalent strain and C is a material constant.

The second category is called 'coupled damage criterion' which indicates that the damage of the material affects the constitutive property of the material. Researchers introduce a damage value D and assume that the real yield stress of the damaged material decreases because of the damage. Then the real yield stress is:

$$\tilde{\sigma} = (I - D)\sigma \tag{22}$$

where, $\tilde{\sigma}$ is the real yield stress of damaged material, D is the damage value and σ is the yield stress of undamaged material.

For a more comprehensive introduction of 'coupled damage criterion', readers can refer to (Lemaitre & Desmorat, 2005).

Due to the complexity in obtaining experimental data for identifying the damage constitutive parameters for the coupled damage criteria, this kind of law was seldom used in industry (Landre et al., 2003). Therefore, a decoupled damage criterion will be utilized in the simulations of the tension and shearing of the riveted joints.

In view of importance of the largest tensile stress, Cockcroft and Latham (1968) have suggested a fracture criterion based on a critical value of the tensile strain energy per unit of volume. The normalised version of this criterion is written as:

$$\int_0^{\bar{\varepsilon}_f} \frac{\sigma_1}{\bar{\sigma}} d\bar{\varepsilon} = C \tag{23}$$

where, σ_1 is the first principal stress.

Assuming that the volumetric strain has a critical value level, Oyane et al. (1980) derived his criterion from a plasticity theory for porous materials:

$$\int_0^{\bar{\varepsilon}_f} (1 - a\frac{\sigma_h}{\bar{\sigma}})d\bar{\varepsilon} = C \tag{24}$$

where, $\bar{\varepsilon}_f$ is the equivalent strain at the fracture point, σ_h is the hydrostatic pressure equal to $-(\sigma_{11}+\sigma_{22}+\sigma_{33})/3$, $\bar{\sigma}$ is the equivalent stress, $\bar{\varepsilon}$ is the equivalent strain and a and C are material constants.

For these kinds of criteria, the parameters have to be determined experimentally. However, in literatures, they are only found successful when applied in similar loading conditions. Tension and shearing of the riveted joints are two different processes where the loading conditions on the rivet are totally different. Hence, an appropriate fracture criterion is essential to predict the fracture in the rivet.

In simulations of tension and shearing of a riveted joint (case a in **Table 1**), both Cockcroft and Latham (1968) and Oyane et al. (1980) criteria are applied to predict fracture. Experimental measurements in tension and in shearing are described in section 6 and 7. For Cockcroft and Latham (1968) criterion, the parameter C is determined as 1.7 in tension and 0.6 in shearing. For Oyane et al. (1980) criterion (a is set as 3), the parameter C is determined as 4 in tension and 1 in shearing. The load displacement curves are shown in figure 8. These results indicate that both these two kinds of criteria are not proper for the rivet material. Therefore, a new fracture criterion has to be developed to predict the fracture both in tension and shearing of the riveted joints.

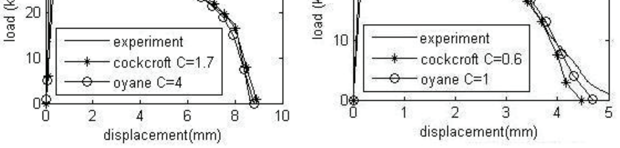

Fig. 8. *Load displacement curves of tension (left) and shearing (right) of riveted joint using Cockcroft and Latham (1968) and Oyane et al. (1980) criteria to predict the fracture.*

Considering that both the first principal tensile stress and the hydrostatic pressure have influence on the fracture of the material, a new ductile fracture criterion is proposed as following:

$$\int_0^{\bar{\varepsilon}_f} \left(a\frac{\sigma_1}{\bar{\sigma}} + b\frac{\sigma_h}{\bar{\sigma}}\right) d\bar{\varepsilon} = 1 \qquad (25)$$

where, *a* and *b* are material constants.

Throughout iterative simulations of both tension and shearing processes of the riveted joints and comparing the results with the experiments, the two parameters *a* and *b* are determined as 1.5 and 1.25. Figure 9 shows the load displacement curves of tension and shearing processes using this new kind of fracture criterion. It can be noticed that the new criterion is capable to predict the fracture in tension and shearing of the riveted joint.

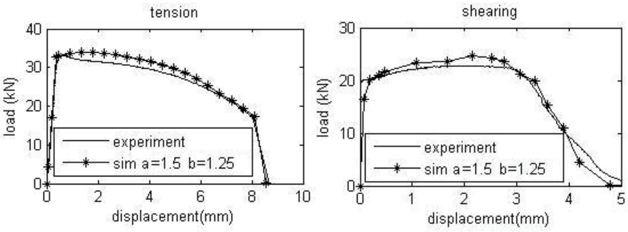

Fig. 9. Load displacement curves of tension (left) and shearing (right) of riveted joint using our new criteria to predict fracture.

6. TENSION OF THE RIVETED JOINTS

6.1. Experimental apparatus

In order to apply the tension of riveted joints, the sheets in the study and the apparatus for tension are shown in figure 10. In experiments, the stroke from the press machine includes mainly three parts: the elastic deformation of the tools and the machine, the deformation of the sheets and the elongation of the rivet. However, in the simulation, only the last two parts exist. Hence, to identify the relationship between the elastic deformation and the force is essential to correct the stroke from the machine. A relatively rigid billet with 40mm diameter is utilized before the tension of riveted joints to obtain the correction equation. The maximum load in the correction test is set as 40kN which is sufficient in all cases. The relationship between the systematic deformation and the force is shown in equation (26).

$$\Delta x = kF \qquad (26)$$

where, Δx is elastic elongation of the tools and the press machine in mm, F is the tensile force in kN and k is a constant value which is identified as 0.035.

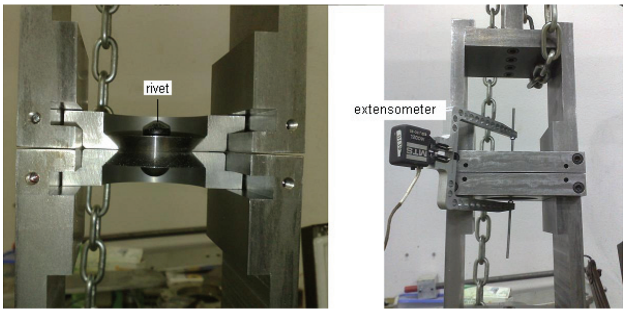

Fig. 10. Experimental apparatus for tension of riveted joints.

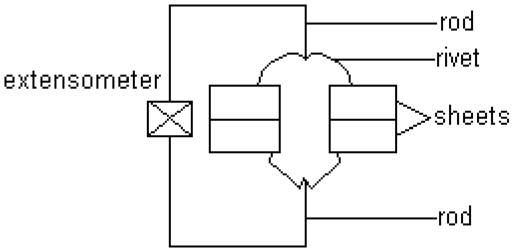

Fig. 11. Illustration of the method to measure the elongation of the rivet in tension process.

To ensure that the correction equation is reliable, a tension test of the riveted joint with 2 relatively rigid sheets is conducted which means the deformation of the sheets can be neglected. Hence, the stroke of press machine includes only 2 parts: the elastic deformation of the press machine and the tools and the elongation of the rivet. The first part can be calculated through equation (26). In order to measure the elongation of the rivet, a small hole is drilled at the centric point of each head respectively which made it easy to fix the two rods of the extensometer, see figure 11 (Wilson & Oliver, 1930). In figure 12, it is obvious that the elongation of the rivet from the extensometer is almost equal to the difference between the stroke and the elastic deformation. The small difference between the two curves may be attributed to the small deformation of the sheets.

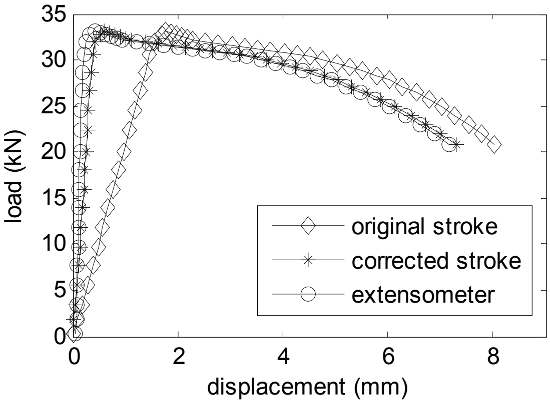

Fig. 12. Verification of the correction equation in tension experiments.

6.2. Results

In experiments, one die is fixed and the velocity of the moving die is set as 2mm/s. For all of the four cases, the fracture occurs in the shank of the rivet. Low deformation level is observed in the sheets during the tensile process for all of the four cases. To simulate the process more accurately, the mesh size in corresponding area is set as 0.3 mm while 0.7 mm for the rest of the part (see figure 13). In the riveting process, the rivet shank is under compressive stress which may change the constitutive property of the rivet material. However, as the strain in the shank is lower than 0.08, we can use as a first approximation the constitutive parameters of the uniaxial tension test of the rivet material in figure 5. Coulomb's friction law is utilized and the coefficient is set as 0.15 between each contacted interface. The ductile fracture criterion is the new one proposed in section 5 and 'kill element' technique (Bouchard et al., 2008) is utilized to eliminate the elements when the damage reaches the threshold value in these elements.

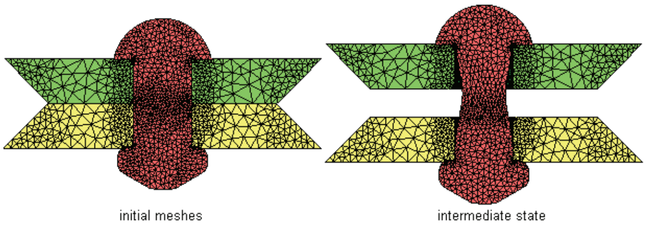

Fig. 13. Meshes settings of the riveted joint in tension process (case a).

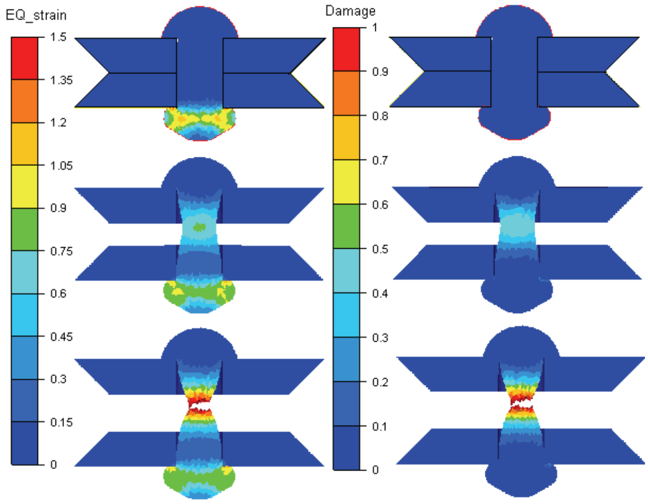

Fig. 14. Equivalent strain distribution (left hand) and damage distribution (right hand) during tension process of the riveted joint (case a).

Figure 14 shows the equivalent strain distribution and damage distribution during tension process of the riveted joint (case a). It can be noticed that the deformation occurs mainly in the shank of the rivet during this process.

Figure 15 shows the load displacement curves during the tension process for all of the four cases. It can be noticed that the curves from the simulations are very close to the ones from the experiments. Each curve can be divided into three parts: OA, AB and BC:

OA: The load increases quickly versus displacement because the displacement includes only the elastic elongation of the rivet and the plastic deformation of the sheets. However, as discussed in part 5, the sheet with 7.8 mm in thickness has almost no plastic deformation in the tension of this kind of riveted joint. In experiments, the contribution to the displacement from the deformation of the sheet with 5.8 mm in thickness is about only 0.7 mm. Hence, the displacement is about 0.5 mm in case a, 1.2 mm in case b, 1.2 mm in case c and 1.9 mm in case d.

AB: The riveting process increases the yield stress of the rivet material and this value reaches or exceeds the maximum tensile stress that the rive shank can bear. Hence, the necking of the rivet shank occurs at point A which makes the load decrease after point A. Because the ductility of the rivet material is relatively high, the displacement in this part is large.

BC: With the elongation of the rivet shank, the fracture occurs at point B and the load decreases sharply until zero.

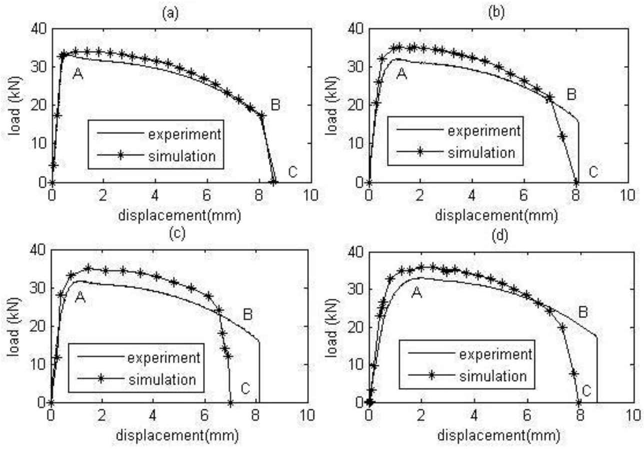

Fig. 15. Load displacement curves of the tension of the riveted joints of all the four cases.

7. SHEARING OF THE RIVETED JOINTS

7.1. Experimental device

The Arcan test procedure (Arcan et al., 1987) is widely utilized to mix and control tensile and shears loads. However, in pure shearing process of the riveted joints, the interaction between the upper die (lower die) and the lower sheet (upper sheet) scratches the lower sheet (upper sheet) and may increase the load remarkably, see figure 16. To avoid this unexpected increment of load, an alternative solution is proposed as shown in figure 17. A rectangular sheet is utilized in the riveting process instead of the round sheet and then in the shearing process, two ends of the sheets are clamped by the press machine to finish the shearing of the riveted joints. The length of the sheet is 300mm and the width is 40mm. For case a, the maximum load from the second experiment is about 23kN while this value in the Arcan test is about 33kN which means that the interaction in zone A and B (in figure 16) increases the maximum load by 43%. Hence, for all of the four cases, this kind of sheet is utilized. The velocity of the press machine is set as 2 mm/s.

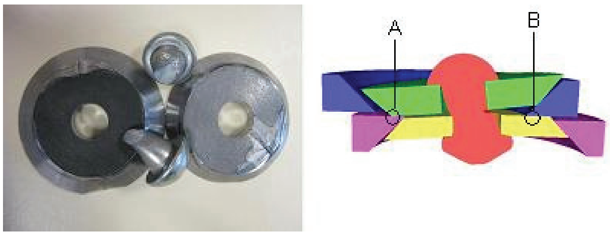

Fig. 16. *Problems in pure shearing of riveted joints using Arcan test procedure.*

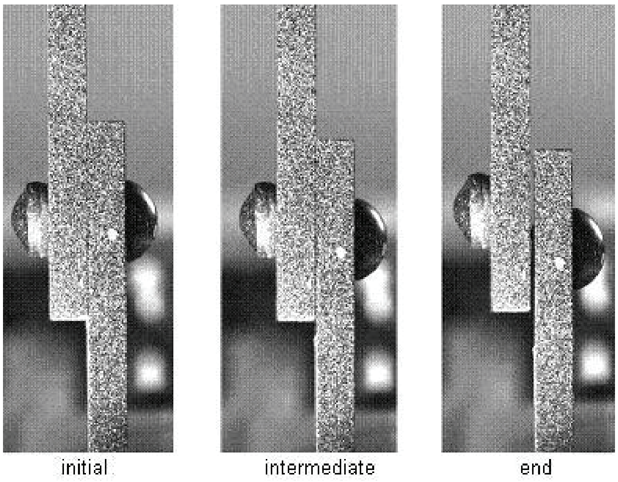

Fig. 17. *Shearing process of riveted joints with rectangular sheets in experiment.*

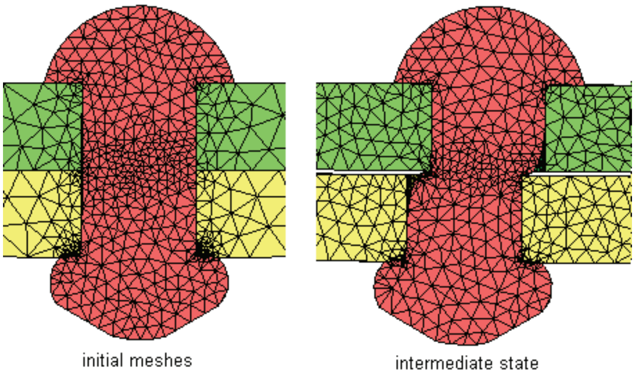

Fig. 18. *Meshes settings of the riveted joint in shearing process (case a).*

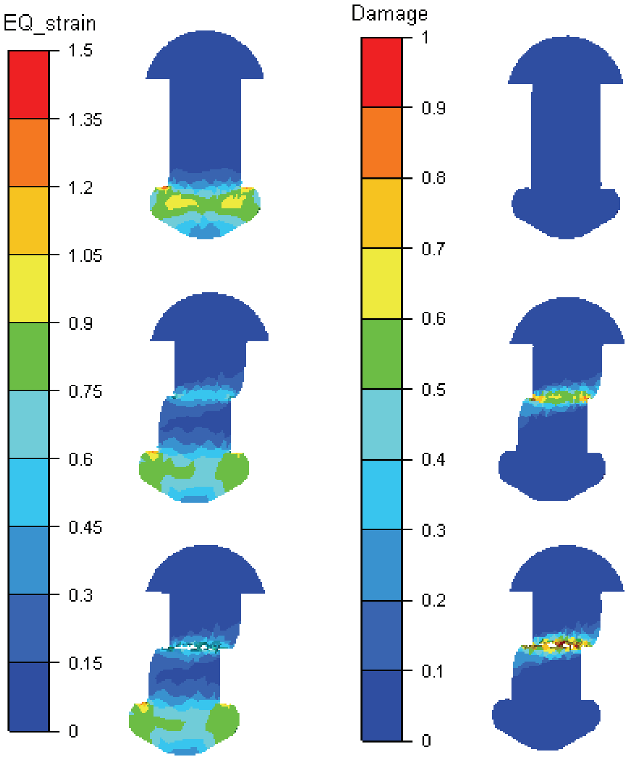

Fig. 19. *Equivalent strain distribution (left hand) and damage distribution (right hand) in the rivet during tension process of the riveted joint (case a).*

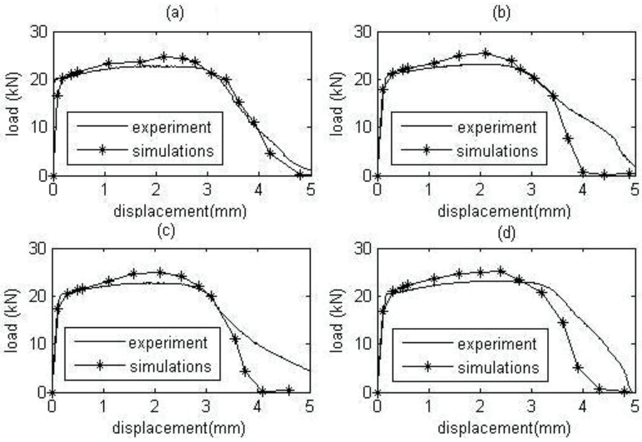

Fig. 20. *Load displacement curves of the tension of the riveted joints for the four cases.*

7.2. Results

In simulations of shearing process of the riveted joints, the settings (including friction, fracture criterion, mesh sizes (see figure 18), etc) are almost the same as those in the tension process detailed in section 6. Figure 19 shows the equivalent strain distribution and damage distribution during shearing process of the riveted joint (case a). It can be noticed that the deformation occurs mainly in the middle shank of the rivet during this process. Figure 20 shows the load displacement curves during the shearing process for all of the four cases. The results from the simulations are quite good as compared with the experiments.

8. CONCLUSIONS

- Experiments of riveting, tension and shearing process of four sizes of riveted joints were achieved and analyzed in this article. Corresponding FEA models were developed and the results from the simulations were in good agreement with the experiment for each process.
- Due to the Bauschinger Effect of the rivet material, uniaxial tension and upset experiments were utilized to obtain the constitutive parameters of the rivet material under tensile stress and under compressive stress, respectively. In riveting process, the constitutive parameters from the upset test were used while in tension and shearing process of the riveted joints, the constitutive parameters of the rivet were from the uniaxial tension of the rivet material. The results showed that it made the simulated results closer to the experimental results.
- As a generalization of the Cockcroft and Latham (1968) and Oyane et al. (1980) ductile fracture criteria, a new criterion was proposed considering both the first principal tensile stress and the hydrostatic pressure to predict ductile fracture of the rivet in tension and shearing process of the riveted joints. Results showed that the new ductile fracture criterion was suitable in these processes for the rivet material.
- Future developments will include experimental identification of a kinematic hardening law of the material of the rivet and the analysis of damage using a non local damage theory.

ACKNOWLEDGEMENTS

This work is a part of the MonaLisa project, financed by Cetim with a close cooperation between Cetim, Cemef and Transvalor. We have to thank Alain Le Floc'h, Francis Fournier and Gilbert Fiorucci for dynamic technical assistance.

REFERENCES

Arcan, L., Arcan, M., Daniel, I.M., 1987, SEM fractography of pure and mixed mode interlaminar fracture in Graphite/Epoxy composites, *ASTM Special Technical Publications*, 948, 41-47.

Blanchot, V., Daidie, A., 2006, Riveted assembly modeling: Study and Numerical characterization of a riveting process, *Journal of Materials processing Technology*, 180, 201-209.

Bouchard, P.O., Laurent, T., Tollier, L., 2008, Numerical modeling of self-pierce riveting - From riveting process modeling down to structural analysis, *Journal of Materials processing Technology*, 202, 290-300.

Boyer, H.E., 1987, *Hardness Testing*, ASM International, USA.

Busby, J.T., Hash, M.C., Was, G.S., 2005, The relationship between hardness and yield stress in irradiated austenitic and ferritic steels, *Journal of Nuclear materials*, 336, 267-278.

Chen, N., Ducloux, R., Pecquet, C., Malrieux, J., Thonnerieux, M., Wan, M., Chenot, J.L., 2010, Numerical and experimental studies of the riveting process, *International Journal of Material Forming* (DOI 10.1007/s12289-010-0987-6).

Cockcroft, M.G., Latham, D.J., 1968, Ductility and the workability of metals, *J. Inst. Met*, 96, 33.

Deng, X., Piotrowski, G.B., Williams, J.J., Chawla, N., 2005, Effect of porosity and tension-compression asymmetry on the Bauschinger effect in porous sintered steels, *International Journal of Fatigue*, 27, 1233-1243.

Fourment, L., 2008, A quasi-symmetric formulation for contact between deformable bodies, *European Journal of Computational Mechanics*, 17, 907-918.

Kelly, B., Costello, C., 2004, FEA modelling of setting and mechanical testing of aluminium blind rivets, *Journal of Material Processing Technology*, 153-154, 74-79.

Landre, J., Pertence, A., Cetlin, P.R., Rodriques, J.M.C., Martins, P.A.F., 2003, On the utilisation of ductile fracture criteria in cold forging, *Finite Elements in Analysis and Design*, 39, 175-186.

Lemaitre, J., Desmorat, R., 2005, *Engineering Damage Mechanics*, Springer-Verlag Berlin Heidelberg.

Oyane, M., Sato, T., Okimoto, K., Shima, S., 1980, Criteria for ductile fracture and their application, *J. Mech. Working Tech*, 4, 66-81.

Ryan, L., Monaghan, J., 2000, Failure mechanism of riveted joint in fibre metal laminates, *Journal of Materials processing Technology*, 103, 36-43.

Tabor, D., 1951, *The Hardness of Metals*, Clarendon Press, Oxford, 105-107.

Wagoner, R.H., Chenot, J.L., 1996, *Fundamentals of metal forming*, John Wiley & Sons, Inc, New York.

Wilson, W.M., Oliver, W.A., 1930, *Tension tests of rivets*, University of Illinois, Urbana.

Zienkiewicz, O.C., Zhu, J.Z., 1987, A simple error estimator and adaptive procedure for practical engineering analysis, *Internat. J. Numer. Methods Engrg.*, 24, 337-357.

NUMERYCZNA I FIZYCZNA ANALIZA WYTRZYMAŁOŚCI POŁĄCZEŃ NITOWANYCH

Streszczenie

Ogólnie obserwuje się dwa rodzaje zniszczenia połączeń nitowanych: przez zerwanie w wyniku rozciągania i przez ścinanie. W celu zbadania tych mechanizmów cztery połączenia o różnych rozmiarach poddano procesom rozciągania i ścinania. Równocześnie opracowano model w programie Forge® 2009, który wykorzystano do symulacji tych połączeń. W symulacjach uwzględniono efekt Bauschingera w materiale co poprawiło dokładność obliczeń. Bazując na kryteriach pękania Oyane i Cockcrofta-Lathama opracowano nowy model pękania, w którym inicjacja i propagacja pęknięcia w połączeniu nitowanym jest przewidywana na podstawie pierwszego naprężenia głównego i średniego naprężenia. Wyniki symulacji są zgodne z wynikami doświadczeń.

Received: July 28, 2010
Received in a revised form: September 27, 2010
Accepted: October 27, 2010